Geometry can provide long-range mechanical guidance for embryogenesis

Mahamar Dicko[1−−4] Pierre Saramito[1,3] Jocelyn Étienne[2,4]

[1]LJK and [2]LIPHY, Univ. Grenoble Alpes, F-38000 Grenoble, France
[3]LJK and [4]LIPHY, CNRS, F-38000 Grenoble, France

Abstract

Morphogenesis is an eminently three-dimensional process, during which an organism undergoes complex deformations to acquire a given shape and organisation. The genetic patterning of Drosophila embryos and the way it regulates the expression of key molecules such as myosin, which can generate local mechanical action, has been well described. However, the way this integrates at the scale of the embryo to drive morphogenetic movements is still to be characterised. Understanding this requires us both to express locally the link between myosin activation and mechanical behaviour, and to calculate globally the resulting force balance and deformations. Axis extension in Drosophila is a good model system for this, since it involves a very large deformation of the whole of the embryo and is crucially dependent on a well characterised anisotropic myosin recruitement pattern. This paper specifically investigates whether this expression pattern causes the observed morphogenetic movement directly or only via the cell intercalation process.

Our prediction of local mechanical behaviour is based on a rheological law which we have recently validated for cortical actomyosin and extend to the case when myosin generates an anisotropic prestress. In order to resolve the stresses and deformations that this produces at the scale of the whole embryo, we develop a novel finite element technique which allows us to solve the three-dimensional mechanical balance resulting from a given global distribution of myosin-generated prestress. Because axis extension is observed to involve in-plane tissue flows, the mechanical problem is expressed as a tangential flow of an emergent fluid on the curved three-dimensional surface of the embryo.

Numerical simulations confirm that the planar-polarised arrangement of myosin in the germband can trigger embryo-scale flows which are qualitatively similar to those observed experimentally. Interestingly, this mechanical behaviour is shown not to rely necessarily on cell intercalation, but rather on the anisotropy of myosin action, which is known to be a major cause of intercalation in general but can also cause cell elongation. We also show that the mechanical balance that leads to axis extension towards posterior is crucially dependent on the geometry of the whole embryo, and specifically on the presence anteriorly of the cephalic furrow, which can act as a guide for morphogenetic movements. This is thus an instance when a prior morphogenetic event, cephalic furrow formation, can modify the mechanical feedback on actomyosin thanks to the geometric dependence of mechanical balance, thus having a cascading influence on further development.

Introduction

Mechanical cues have been shown to influence cell and organism phenotypes, through mechanisms of mechanosensation and mechanotransduction [1, 2, 3]. At the cell scale, it has been shown that the mechanical properties of the environment could lead to a self-organised polarisation of the cytoskeleton [4] and to a different cell morphology through collective dynamics of cytoskeletal molecules [5], independently of a signaling pathway activated by transduction. In the case of a whole organism, this type of mechanical driving of morphological phenotype is of high interest, since the mechanics provide an alternative route to whole-organism coordination and function as opposed to diffusion and transport of chemical factors. In the context of embryogenesis, the notion of *extrinsic forces* has been introduced [6] to highlight the fact that mechanical tension equilibrates over the size of the whole embryo and can thus be felt far from the location where biochemical energy has been converted to mechanical action.

Here we focus on how the extrinsic forces integrate at the scale of the whole embryo in order to achieve the correct deformation. This integration of forces is crucially dependent on the geometry, which is itself the product of previous morphogenetic movements. The fundamental concept here is Newton's third law of action and reaction. In the context of early *Drosophila* embryogenesis, this law turns out to have implications of direct practical interest in the analysis of observations, because the interactions of the embryonic epithelial tissue with other structures is very limited: there is no specific adhesion on neighbouring vitelline membrane, and no matrix basally. This implies that the mechanical balance applies to the embryonic tissue as an isolated system, or a nearly isolated system: as in tensegrity structures, the external forces are dominated by internal ones. In addition, because of the small scale and high viscosity of the tissue, inertial forces are negligible, thus Newton's second law yields that, locally also, all forces are quasi-instantaneously balanced: together, this implies that there is a quasi-instantaneous equilibration of mechanical tension all across the embryonic tissue. Mechanical tension is thus an efficient messenger with properties that are very complementary to diffusion of biochemical factors. One additional interesting fact in this respect is the crucial role of geometry in the mechanical balance established, see figure 1*e* for an example at human scale. At the embryo scale too, geometry can be used to obtain very different mechanical balances in the same material and with the same driving force. Thus, some geometrical features having arisen from previous morphogenetic movements can crucially affect how subsequent morphogenetic events can be driven by extrinsic forces. Such an effect is visible for instance for the head involution of *Drosophila*, which necessitates a sucessful dorsal closure to be complete [7].

Specifically, this paper addresses the question of the driving of germ-band (GB) extension by the activity of myosin during Drosophila development. During a 90-minute process, the GB narrows in the dorso-ventral (DV) direction, which is referred to as *convergence*, and simulatenously incurs *extension* in the antero-posterior (AP) direction, see figure 1*a*,*b* [8]. This extension however is not occurring in a symmetric way towards the anterior and posterior ends of the embryo: it is very markedly oriented towards the posterior.

Two causes contribute to this extension: within GB, myosin is organised in a so-called planar-polarised manner, along cell-cell junctions aligned with the DV direction [9, 10]. Ultimately this is shown to lead to cell intercalation, from a mechanical point of view it thus has to exert a tensile stress in the DV direction. Concurrently at a separate location, under the action of myosin which lacks planar polarisation, the posterior endoderm invaginates as a funnel-shaped tube, the posterior midgut (PMG), see figure 1*a*,*b*. It has been shown [11, 12, 13] that either of these phenomena in the absence of the other could cause GB extension, although to a different extent and with different characteristics (exhibiting more or less cell intercalation and shape change).

In this paper, we present numerical simulations of the mechanical process during GB extension. For a given distribution of myosin at the apices of cells, we solve mechanical balance equations and obtain a prediction of the velocity with which these apices will move. This differs in nature from previously published approaches for tissue mechanics. Compared to vertex models [reviewed in 14], the tissue is treated as a continuum made of the apical actomyosin of each cell mechanically connected to neighbouring cells via adhesive contacts. This modelling approach, while it does not allow to distinguish cell deformation and rearrangement contributions within the tissue strain [15], has the advantage of introducing fewer parameters while retaining the main phenomenology of developing epithelia. Continuum approaches have been used by

several modelling works for ventral furrow formation [reviewed in 16], and also for GB extension in one work [17]. However, continuum approaches so far have not attempted to use the pattern of myosin activation as the phenomenon originating in the driving force of the simulated deformations, but have rather been focusing on integrating the observed cell-intrinsic phenomenology into tissue-scale deformations. Our approach in this paper is to bypass the cell scale and cell-intrinsic phenomenology, and assess how much of tissue-scale deformations can be predicted directly from the pattern of myosin activation only. The underlying question is whether it is mechanically plausible that the patterns of myosin activation in different mutants can alone give rise to the corresponding morphogenetic movements.

Our modelling is based on some mechanical assumptions on how the apical actomyosin in the developing epithelium interacts with its environment, and on a rheological model of actomyosin itself [5]. The numerical simulation of flows on a curved surface is based on a novel finite element technique, which is not limited to potential flows as in previous literature [18], and for which we have proven convergence properties [19]. Our numerical results confirm that an anisotropic myosin contractility (mimicking its planar-polarised recruitment) in the GB leads to an extension flow along the AP direction. We also focus on the effect of the invaginating posterior midgut on GB extension, and on the long-distance influence of the embryo geometry at the time of GB extension.

Additionally, numerical simulations allow us to test the role of geometry on the flows that result from myosin action. We note that, when posterior midgut contraction is not happening, the distribution of myosin is close to symmetrical along the AP direction. However, the flow observed is markedly towards the posterior even in this case. The most prominent nonsymmetrical feature of the embryo at this stage is the presence of the cephalic furrow (CF), a trough that loops around the embryo dorso-ventrally, whereas no such structure perturbs the smoothness of the embryo surface at the other limits of the GB. Although mutants exist that do not form a cephalic furrow [21], the consequences of this on GB extension has not been specifically studied. Using numerical simulations, we show that the cephalic furrow can act as a barrier for deformations and guide myosin-driven convergence and extension towards the posterior end.

Results

A continuum shell model of the apical acto-myosin and adherens junctions structure can produce convergence and extension flows

It is believed that the structure driving the morphogenetic movements in early embryos is the apical acto-myosin. Indeed, it has been shown [20] that the movements of the whole embryo during gastrulation and early GB extension could be predicted accurately by the sole knowledge of the displacements of the apical acto-myosin through time, the other structures (cell cytoplasms, nuclei, membranes, and yolk, see figure 1*c*,*d*) being passively deformed as a viscous medium. This is consistent with the observation that all morphogenetic movements are mediated by myosin. From a physics perspective, this means that the source of mechanical energy in the system is the conversion of biochemical energy by myosin.

Apical acto-myosin, which is located within 1 μm of the cell's apices, is connected from one cell to the other by transmembrane adherens junctions. From a mechanical point of view, the embryo should thus be seen as a thin shell of apical acto-myosin seamed together by adherens junctions, surrounding a viscous-like medium. Apical acto-myosin organisation, figure 2*c*, is either junctional (i.e., lining cell-cell junctions within each cell) or medial (i.e., lining the apical membrane), and can have an anisotropic organisation within each cell. In normal development, there is no disconnection within the embryo-wide structure constituted by acto-myosin and adherens junctions: forces are transmitted across cell-cell junctions via the adherens junctions, and the whole of this structure forms an embryo-wide shell. This shell is bound to the apical plasma membranes, making this compound structure mostly impermeable, but, as stressed in the introduction, it has little mechanical interaction with its environment. On the outer side of the apical shell is the perivitelline membrane, but no specific adhesions bind them together, and the perivitelline liquid can play the role of a lubricating fluid between the two. On the inner side, the passive behaviour of the cell cytoplasms and basolateral membranes implies that they are felt only as a drag (viscous friction). This results in a friction

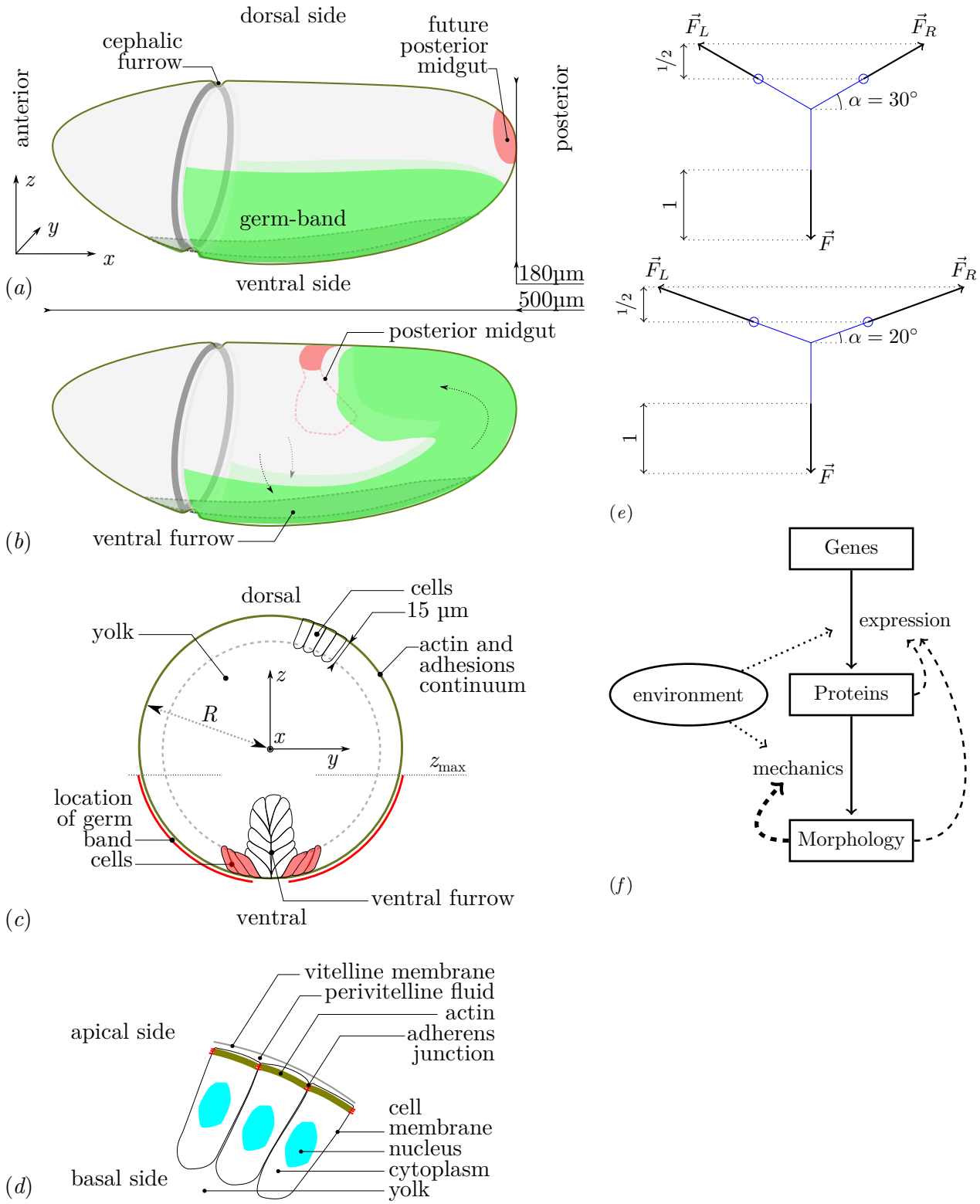

Figure 1: See caption on next page

Figure 1: (*a*) Geometry and tissue configuration of *Drosophila* embryo [6] immediately prior to GB extension. Tissues situated at the outer surface are in solid colors, dashed lines correspond to structures internal to the embryo. (*b*) Sketch of morphogenetic movements and tissue configuration during GB extension and PMG invagination. (*c*) Geometry and structures of mechanical relevance in a transverse cut. The coordinates origin is in the center. Contiguous cells form a continuous surface at the periphery of the embryo, the external limit is the cell's apical side, the internal one (dashed line) their basal side. Only some cells are drawn. On the ventral side, a ventral furrow forms before GB extension and seals at the ventral midline just as the GB starts extending. Within the cells, actin structures form apically and are connected from one cell to the other by adhesive molecules, forming an embryo-scale continuum at the periphery of the embryo. The GB is highlighted in red, in this region myosin is activated in a planar-polarised manner. (*d*) Sketch of structures of mechanical relevance in the epithelial cells. The *vitelline membrane* is a rigid impermeable membrane. The *perivitelline fluid* is incompressible and viscous. The *actomyosin* of *Drosophila* cells is located at their apical surface, it is a thin layer (< 1 μm) connected to other cell's actomyosin via *adherens junctions*. The *cytoplasm* of cells behaves as an incompressible viscous fluid during the flow [20]. It is enclosed in the cell membranes, which have a low permeability but present excess area compared to cell's volume. Beyond the basal surface of the cell monolayer, the *yolk* is an incompressible viscous fluid. (*e*) Example of the influence of geometry on forces. The same Y-shaped system of ropes (blue lines) is arranged in different geometries (angle α) and is otherwise identical. When subjected to a force $\vec{F}$, mechanical balance requires that the forces at the anchorages (blue circles) are such that $\vec{F}_L + \vec{F}_R = -\vec{F}$. This leads to a behaviour of the magnitude of forces at anchorages as $1/\tan\alpha$. (*f*) Current global morphology as an additional feedback on genotype control on phenotype. In addition to the well known feedbacks of biochemical phenotype (protein expression) and morphological phenotype (mechanotransduction) on gene expression (thin dashed arrows), we explore here a direct mechanical feedback (bold dashed arrow) of currently achieved morphology (i.e., presence of cephalic furrow) on the way genetically-controlled protein expression (i.e., myosin activity pattern) controls future morphogenetic events (i.e., GB extension).

force per unit area proportional to the product of the velocity $\boldsymbol{v}$ by a friction coefficient c_{f}. In terms of forces, the balance of the forces tangentially to the surface is thus:

$$\boldsymbol{\nabla}_\Gamma \cdot \boldsymbol{\sigma} = c_{\mathrm{f}} \boldsymbol{v}. \tag{1}$$

The stress tensor $\boldsymbol{\sigma}$ is the tension in the apical shell of geometry Γ, and $\boldsymbol{\nabla}_\Gamma \cdot$ is the surface divergence operator [22]. In order to obtain a *closed* model (i.e., a self-sufficient one), we need to supplement mechanical balance with a material law which links the stress to the deformations of the apical shell, and, in the present case, to the myosin activity also. We have recently derived and validated such a material law [5] by quantitative comparison of predictions of forces exerted by actomyosin cortex of single cells with experimental measurements. In a linear approximation, the apical actomyosin of embryos can be expected to have a similar material law [23], which can be written in the general form:

$$\tau_\alpha \overset{\triangledown}{\boldsymbol{\sigma}} + \boldsymbol{\sigma} - 2\eta \dot{\boldsymbol{\varepsilon}}(\boldsymbol{v}) - \eta_{\mathrm{b}} (\nabla_\Gamma \cdot \boldsymbol{v}) \mathbf{P} = \boldsymbol{\sigma}_{\mathbf{a}} \tag{2}$$

where τ_α is the relaxation time of acto-myosin, $\overset{\triangledown}{\boldsymbol{\sigma}}$ the objective derivative of the stress tensor, η and η_{b} are effective shear and compression viscosities of acto-myosin, and

$$\dot{\boldsymbol{\varepsilon}} = \frac{1}{2} \left(\nabla_\Gamma \boldsymbol{v} + \nabla_\Gamma \boldsymbol{v}^{\mathrm{T}} \right)$$

is the rate-of-strain tensor. The tensor $\boldsymbol{\sigma}_{\mathbf{a}}$ describes the myosin contractility, and can be understood as a prestress: because of myosin action, the meshwork of actin is continuously being offset from its stress-free configuration. The pre-stress is proportional to the myosin concentration and rate of power strokes [5, 23], and $\mathbf{P}$ is the projection tensor onto Γ, which is also the identity tensor on the surface. The relaxation time was found to be around 15 minutes in this previous work, which means that for the 90-minute germ band extension process we are interested in times longer than relaxation. We have also shown for similar equations in another biophysical context and in one dimension [24] that the term $\tau_\alpha \overset{\triangledown}{\boldsymbol{\sigma}}$ did not introduce marked qualitative features to the flow for time scales as short as the relaxation time itself. For the sake of simplicity, we will thus neglect the term $\tau_\alpha \overset{\triangledown}{\boldsymbol{\sigma}}$ in what follows.

With this hypothesis, the mechanical balance equation 1 and the constitutive equation 2 can be combined into a single equation:

$$\boldsymbol{\nabla}_\Gamma \cdot \boldsymbol{\sigma}_{\mathbf{a}} = -2\eta \nabla_\Gamma \cdot \dot{\boldsymbol{\varepsilon}}(\boldsymbol{v}) - \eta_{\mathrm{b}} \nabla_\Gamma \nabla_\Gamma \cdot \boldsymbol{v} + c_{\mathrm{f}} \boldsymbol{v} \tag{3}$$

On the left-hand side of equation 3 is the myosin term, which provides the energy for the motion. On the right-hand side are two terms corresponding to energy dissipation: forces of friction with the actomyosin's environment, and the viscous forces, corresponding to the cost of deforming the apical shell. These do not distinguish between inter-cellular dissipation, i.e. the mechanical energy spent during cell rearrangements in breaking cell-cell adhesive bonds and the one gained when establishing new ones; and intra-cellular dissipation, such as the cost of deforming the actomyosin cortex. Rather, these are lumped together, and taking a linear approximation, represented by effective viscosities η and η_{b}.

The myosin contractility term $\boldsymbol{\sigma}_{\mathbf{a}}$ is the source term that provides energy to the system and causes the deformations. We have shown theoretically and verified experimentally [5, 23] that to a first approximation it is proportional to the local myosin concentration. However, when myosin is preferentially recruited along anisotropic actin structures, the tensor $\boldsymbol{\sigma}_{\mathbf{a}}$ is also anisotropic [Supplementary materials in 5], and can be decomposed into a spatially-dependent intensity σ_{a} and an orientation tensor $\mathbf{A}$, $\boldsymbol{\sigma}_{\mathbf{a}} = \sigma_{\mathrm{a}} \mathbf{A}$. In the case of GB extension, it is observed experimentally [9, 10, 25] that myosin is activated in the GB, thus $\sigma_{\mathrm{a}} > 0$ in the GB, and is recruited along DV-oriented cell junctions, thus $\mathbf{A} = \boldsymbol{e}_{\mathrm{DV}} \otimes \boldsymbol{e}_{\mathrm{DV}}$, see figure 2.

Using the numerical technique described in appendix , we obtain numerical approximations of the solution of this problem for a geometry Γ closely mimicking the shape of *Drosophila* embryo, see appendix . Figure 3 shows an example of a simulation result. The green colour codes $\sigma_{\mathrm{a}}(\boldsymbol{x})$, the location where myosin is

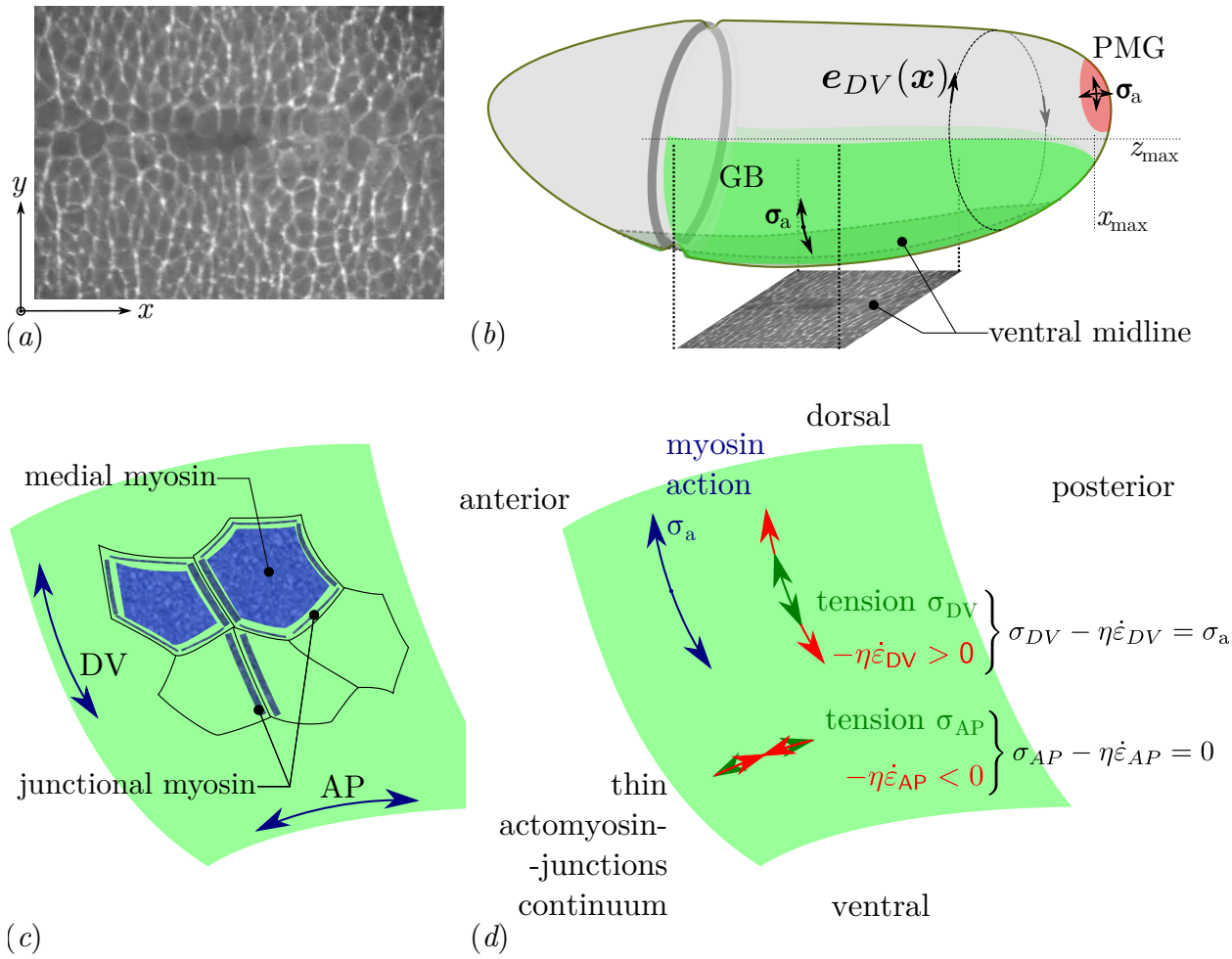

Figure 2: Myosin distribution during GB extension. (*a*) Fluorescently labeled myosin in the GB and midline over a ventral region, reprinted from [25]. The myosin is significantly denser along DV-oriented cell junctions (y direction) than along AP-oriented ones (x direction). This planar polarisation can be quantified [9, 26, 25]. (*b*) Sketch of the geometry of the entire embryo with the planar-polarised GB region (*green*) and the isotropically contracting PMG region (*red*) [6]. The region shown in panel *a* is shown from below. Isotropic contraction is assumed to be linked with an isotropic action of myosin, thus $\boldsymbol{\sigma}_\mathbf{a}$ is an isotropic tensor in the PMG, whereas planar polarisation results in an anisotropic prestress $\boldsymbol{\sigma}_\mathbf{a}$ [5], whose orientation we take as $\boldsymbol{e}_{\mathrm{DV}} \otimes \boldsymbol{e}_{\mathrm{DV}}$, where $\boldsymbol{e}_{\mathrm{DV}}$ is a tangential unit vector orthogonal to the main axis of the embryo. (*c*) Sketch of the different pools of myosin present at the cell apices. Junctional myosin is associated with cell-cell junctions, and may form supracellular cables. Medial myosin is apical myosin not associated with junctions. (*d*) Tangential apical stresses in an arbitrary region of the GB. According to the constitutive relation, equation 2, the (opposite of) viscous stress $-\eta\dot{\boldsymbol{\varepsilon}}$ and mechanical stress $\boldsymbol{\sigma}$ need to balance the myosin prestress $\boldsymbol{\sigma}_\mathbf{a}$ in both AP and DV directions. Since myosin prestress is zero along AP, the mechanical stress is equal to the viscous stress in this direction, $\sigma_{\mathrm{AP}} = \eta\dot{\varepsilon}_{\mathrm{AP}}$, thus AP tension results in extension. In the DV direction, we have $\sigma_{\mathrm{DV}} - \eta\dot{\varepsilon}_{\mathrm{DV}} = \sigma_{\mathrm{a}}$, resulting in a combination of DV tension and contraction (convergence). The global mechanical balance, equation 1, has to be solved in order to calculate $\boldsymbol{\sigma}$ and $\dot{\boldsymbol{\varepsilon}}$.

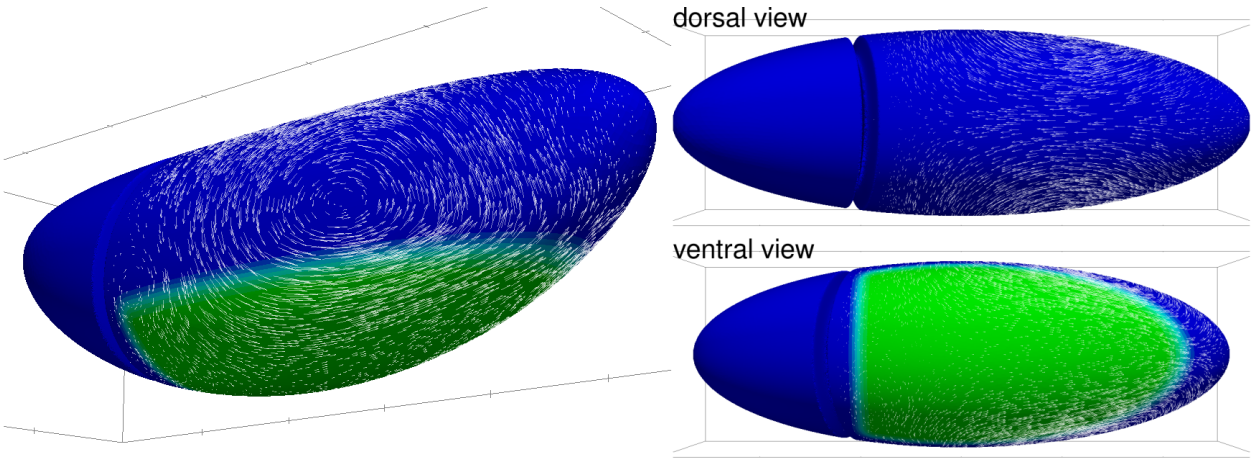

(*a*)

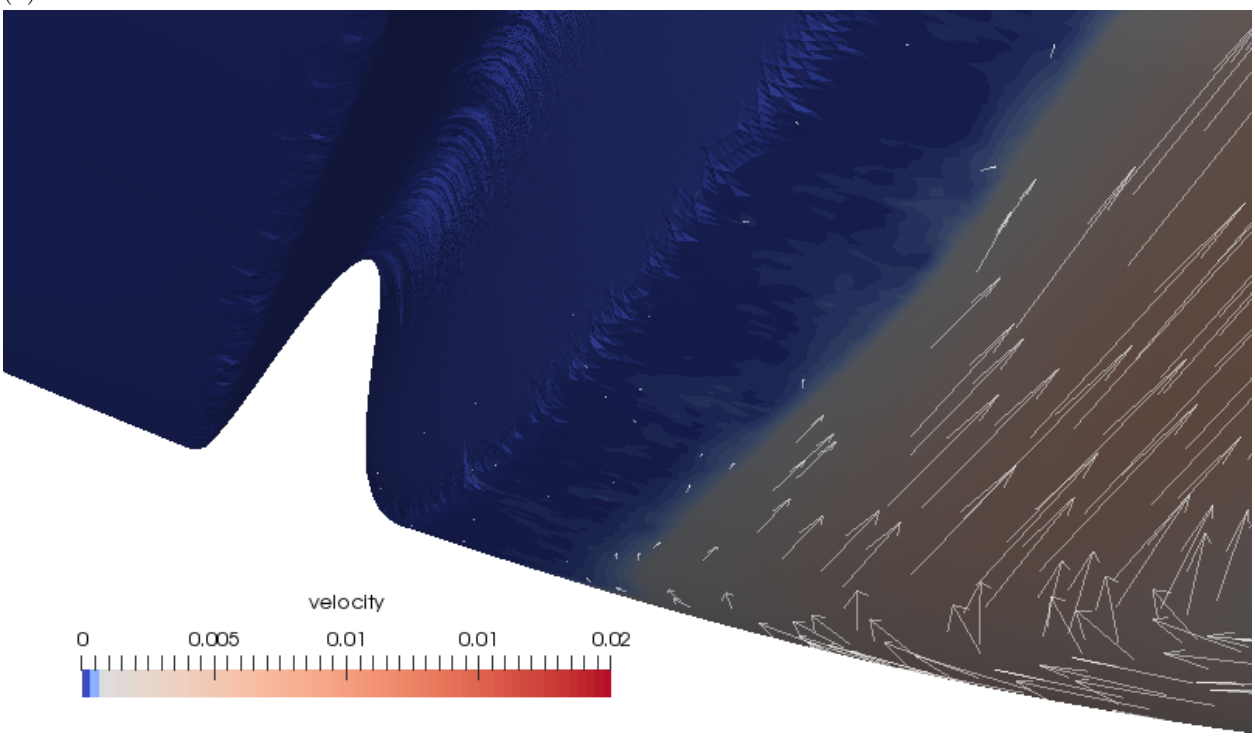

(*b*)

Figure 3: Flow field generated by planar-polarised myosin contractility in the GB. Parameters are $\eta_{\mathrm{b}}/\eta = 10^3$, $c_{\mathrm{f}}/\eta = 1/R$, where R is the radius of a transverse cut of Γ, see figure 1*c*. The GB region is defined as the ventral region posterior to cephalic furrow, and more ventral than a coronal plane $z_{\max} = -0.2R$, see figure 1. (*a*) Global view. The cephalic furrow is represented by a trough, the ventral furrow is not represented as we assume it to have sealed completely at the time corresponding to the simulations. Green, ventral region of the GB where we assume myosin planar-polarised contractility. White arrows, velocity vectors (arbitrary units, not all vectors calculated are represented). (*b*) Close-up of the region close to cephalic furrow and ventral midline. Every velocity vector calculated is represented, in arbitrary units 10 times larger than in panel (a).

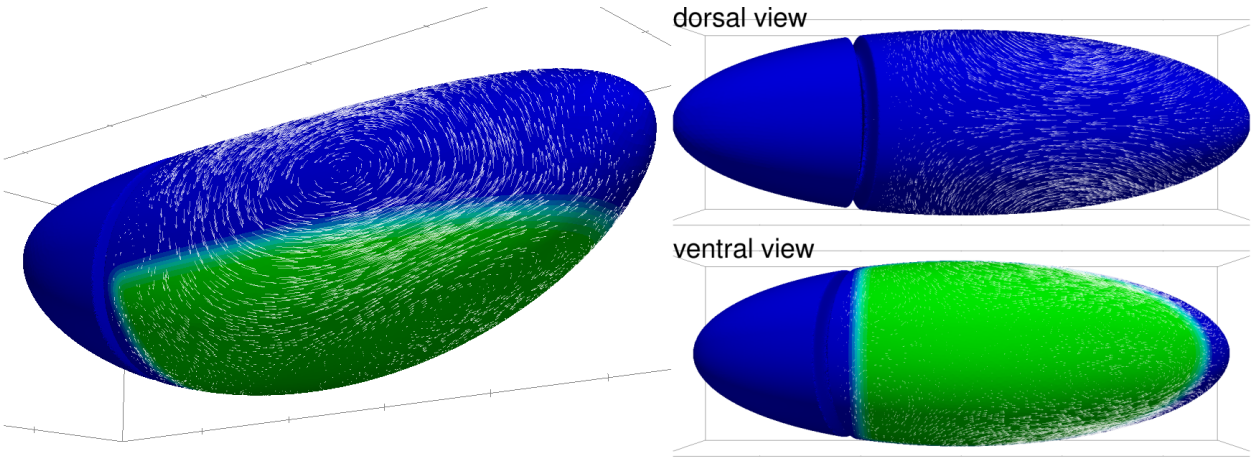

(a)

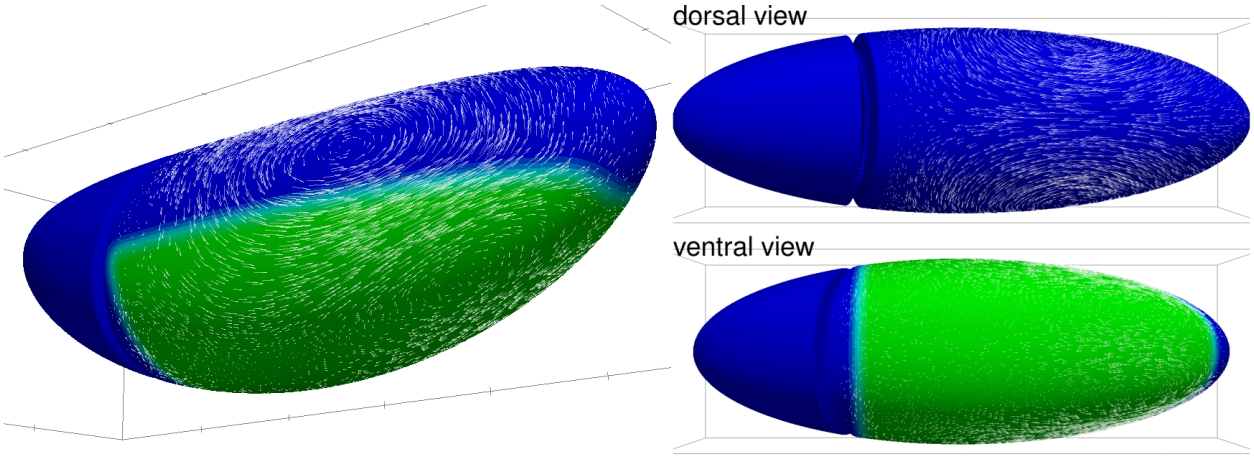

(b)

Figure 4: Flow field generated by planar-polarised myosin contractility in the GB. Parameters are the same as in figure 3, but the region of planar-polarised myosin recruitment is larger: (a) $z_{\max} = 0$, (b) $z_{\max} = 0.2R$ (compare to figure 3 where $z_{\max} = -0.2R$). The same phenomenology is observed, with a strong posterior-oriented GB extension. Close to the midline, the tissue is not extended and goes towards anterior (slightly for $z_{\max} = 0$, significantly for $z_{\max} = 0.2R$).

activated along dorsoventral direction $\mathbf{A} = \boldsymbol{e}_{DV} \otimes \boldsymbol{e}_{DV}$, and the arrows are the predicted velocity of the surface displacement of the apical continuum. This predicted flow is strongly dominated by two laterally-located vortices, which have their center slightly dorsal from the edge of the GB region. They are rotating such that the velocity in the GB is strongly towards the posterior, as is the case in *Drosophila* GB extension. The tissues situated dorsally (amnioserosa) are predicted to be strongly deformed by the vortices, this is indeed the case in *Drosophila* development, although two other morphogenetic events are not included in this simulation, namely formation of dorsal folds and post-midgut invagination (see below). On the whole, the flow obtained is very similar to what is observed during *Drosophila* GB extension.

Note that we impose mathematically that velocities are tangential with the embryo surface (see appendix). Indeed, this is what is observed in experiments, we have thus made the simplifying choice of assuming this rather than try to predict it. A model bypassing this hypothesis would need to be significantly more complicated, as the force balance in the normal direction would need to be calculated in addition to the one in the tangent plane. This force balance should include the pressure difference between the periviteline liquid and the embryo interior beyond the apical membranes (yolk and cytoplasms) and the viscous drag from these structures, and also the tension and bending forces in the cell apices. Although we do not model this, the force needed to keep the flow tangential in our simulations is calculated, and is the Lagrange multiplier associated with the tangentiality constraint.

The complementary role of planar-polarised myosin and post-midgut invagination

It has been shown [11, 12, 13] that GB extension is not solely due to the action of planar-polarised myosin within the GB, but also to the pulling force that another morphogenetic movement causes, namely the invagination of endoderm in the posterior region, also called post-midgut (PMG) invagination.

Our present numerical approach does not allow us to simulate deformations of the surface in the normal direction, which would be necessary to simulate the PMG invagination process. However, it is possible to mimick the effect of PMG invagination on neighbouring tissues by simulating an in-plane isotropic contraction of the PMG tissue, figure 2*b*. Figure 5*e* shows that this does generate an extension of the GB area, although the deformation on the dorsal side is greater in this case. Combined with planar-polarised myosin action in the GB, figure 5*b*–*d* shows that PMG invagination does modify the flow pattern substantially and provides a complementary cause of GB extension, consistently with the experimental studies cited above. In fact, because of the linearity of equation 1–2, the superposition principle applies and the flows shown in figure 5*b*–*d* can be written as the weighted sum of the flows with planar-polarised myosin only, figure 5*a*, and PMG invagination only, figure 5*e*.

Influence of the geometry of genetic patterning

Although *in toto* imaging of *Drosophila* embryos is now possible using SPIM [27, 28, 13], a global cartography of myosin activation during GB extension is still missing, and the precise location of myosin activation is not available. We thus tested several configurations of the extent of the GB zone in which myosin is expressed, figure 4. We find that the global flow is relatively robust with respect to the precise myosin patterning, and GB extension is consistently obtained. However, some features vary, and in particular an anterior-wards backflow develops along the ventral midline when the myosin activation zone extends more laterally. These backflows are attenuated or may disappear when the PMG contraction is large enough. These backflows are not observed experimentally, although mutants such as *torsolike* that present planar-polarised myosin but not PMG invagination form ectopic folds in the germband, which could be due to a buckling phenomenon [13].

Influence of the choice of the mechanical parameters

The material parameters of the cortical actomyosin in *Drosophila* are not known, and quantifying them experimentally is very challenging [23], since this early step of development requires the presence of the

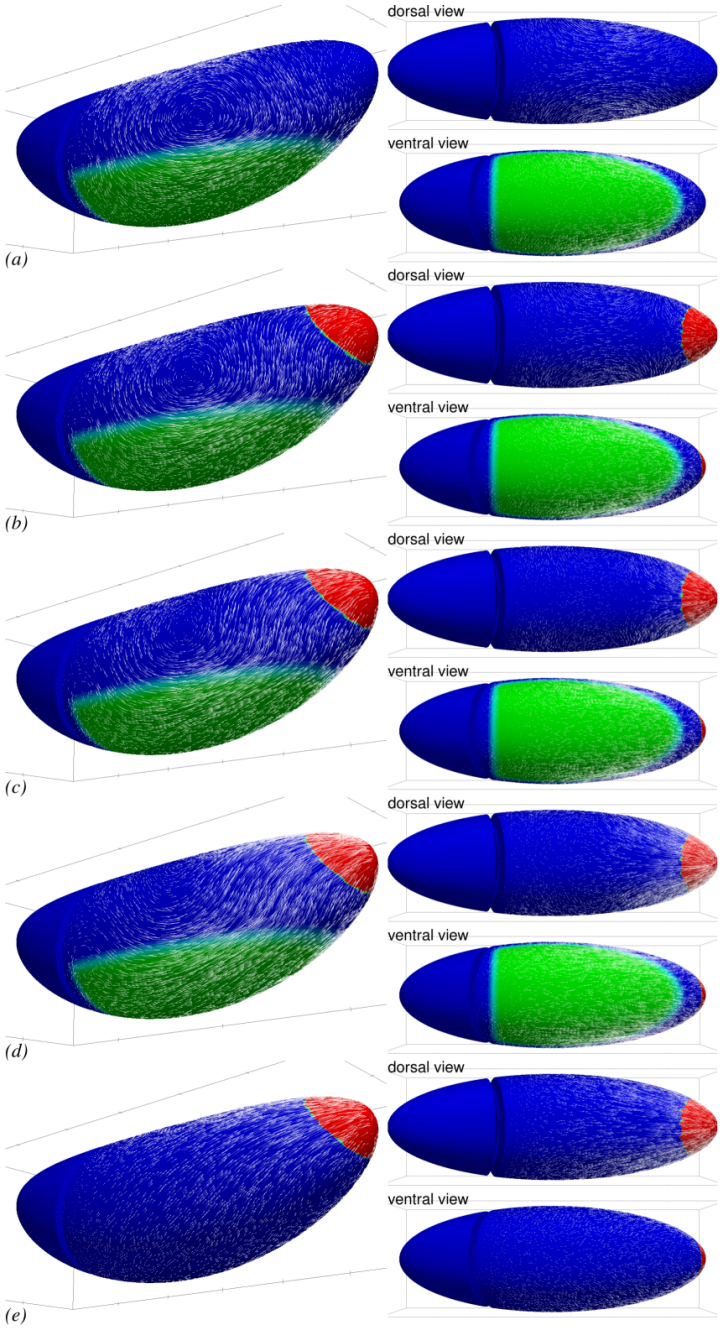

Figure 5: PMG invagination can contribute to GB extension. Parameters are the same as in figure 3, reprinted in (*a*), but (*b*–*e*) another region (red) is actively contracting in an isotropic way, mimicking the effect of PMG invagination on neighbouring tissues. From (*b*) to (*d*), the isotropic PMG contraction intensity is doubled each time. (*e*), effect of isotropic PMG contraction in the absence of any myosin activity in the GB itself.

rigid vitelline membrane that surrounds the embryo and prevents direct mechanical measurements from the exterior. Magnetic tweezers have been used [3], but the magnetic particles were not directly associated with the actomyosin cortex and thus measured other mechanical properties than those required by our model. Laser cuts can provide valuable information on the evolution of tension [29] or its anisotropy [13]. By comparison with a model of subcellular actomyosin, its material parameters can be obtained (medial actomyosin relaxation time, shear viscosity and friction coefficient) [30]. However, these values are not necessarily the ones needed for our system, as they correspond to a subcellular system while we focus on the tissue scale. Indeed, although the model in [30] is formally identical to equation 1–2, their estimated viscosity does not include tissue-scale viscous-like costs, and their friction coefficient includes the friction cost of movements of the actomyosin cortex relative to the cell membrane, whereas both apical membranes and actomyosin cortices flow in GB extension. Therefore, rather than setting the parameters to measured values in our simulations, we verify the robustness of our model predictions over a large range of parameter values.

Four parameters appear in equation 3: the magnitude of myosin prestress σ_a, the friction coefficient c_f, and the two viscosities η_b and η. Two of these parameters, σ_a and η, set respectively the magnitude of stresses and velocities, leaving two free parameters: η_b/η, which is nondimensional; and c_f/η, which is the inverse of the hydrodynamic length Λ.

The ratio η_b/η compares the bulk to the shear viscosity: if it is very large, then the flow will be nearly incompressible in surface, meaning that any surface element (and in particular, any cell) will conserve the same area through flow, and hence all deformations will be locally pure shear deformations. If the ratio is small, then the viscous cost of locally changing the apical area will be similar to that of pure shear, and, depending on the global force balance, area changes may dominate. Indeed, if η_b/η is $2/3$ (such that the Poisson ratio is zero), then a unixial load (such as a perfectly planar-polarised myosin action could be supposed to produce) will result in an area change only and no pure shear at all, or, in developmental biology terms, in convergence only and no extension. This effect is illustrated in figure 6, where η_b/η covers the range 10 to 10^3. In the latter case, the negative DV strain rate (convergence) exactly balances the positive AP strain rate (extension), whereas in the former case, convergence strongly dominates. The strain rates in all cases are not uniform across the ventral side depending on the AP position, with a marked decrease of the pure shear in the central part of the GB, however other factors are seen to affect this spatial distribution in the rest of the paper. Between $\eta_\mathrm{b}/\eta = 10$ and $\eta_\mathrm{b}/\eta = 100$, there is a switch from area-reduction dominated flow (area reduction rate 4 times AP strain rate) to a shear-dominated flow (area reduction rate of the same order as AP strain rate). Experimentally in *Drosophila* embryos, the deformations are not limited to pure shear but include some area change [11], so by comparison with our numerical result, the correct order of magnitude of η_b/η can be expected to be of the order of 10 to 100. This is much larger than the ratio 3 that could be expected from a simple 3D-isotropic modelling of actomyosin [30], probably because of the anisotropy of actomyosin meshwork, and possibly of active processes that may regulate the cortex thickness and density.

The hydrodynamic length $\Lambda = \eta/c_\mathrm{f}$ is the characteristic length beyond which shear stress transmitted within the actomyosin will be screened by friction with the exterior: it thus determines the length over which the effects of a force are felt. It is of interest to test the effect of a hydrodynamic length either much larger, much smaller or comparable to the size of the embryo (R, the radius of a transverse section, figure 1). The results shown in figure 7 show how the action of myosin gives rise to a more local flow pattern when the hydrodynamic length is small. This localisation is around the areas in which there is a *gradient* of myosin activity, indeed in areas of uniform myosin activity, the resulting effect is a uniform tension (see a similar effect in models of cells plated on a substrate, e.g. [24, Fig. 3b]). It can be seen on figure 7*b*,*c* that indeed the strain variations are more abrupt when hydrodynamic length is small, whereas the long range interations allowed by a very large hydrodynamic length give rise to an embryo-scale flow. On the whole, flows which reproduce experimental observations better are obtained when Λ is of order 1 or more, that is, the hydrodynamic length is comparable to or larger than the GB width in DV. This is consistent with the order of magnitude of hydrodynamic lengths found by laser ablation in other systems [30], although in laser ablation the likely contributions to friction differ for a part, since the recoiling actomyosin is likely

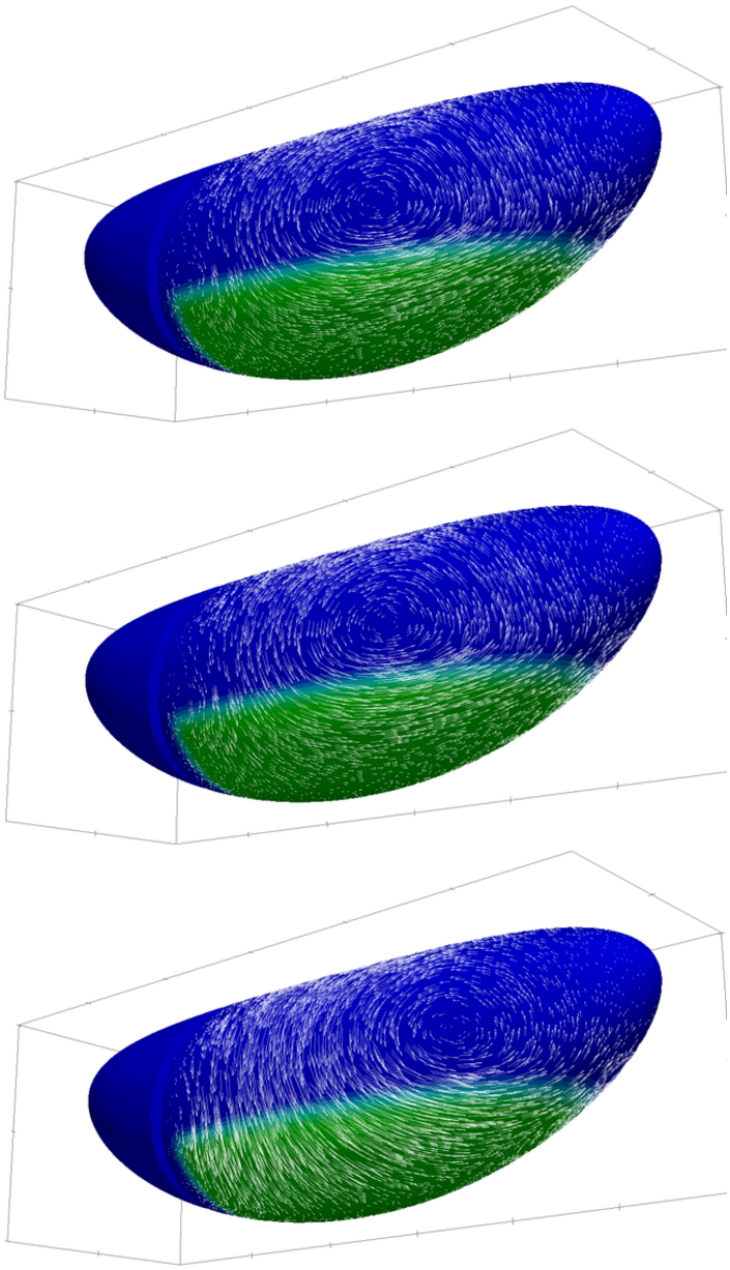

(*a*)

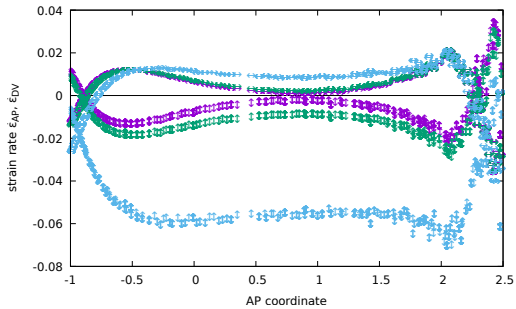

(*b*) DV and AP strain rates

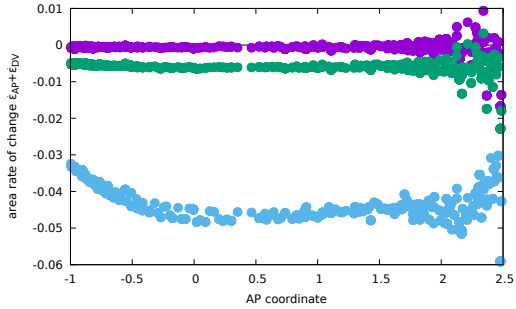

(*c*) Area rate of change

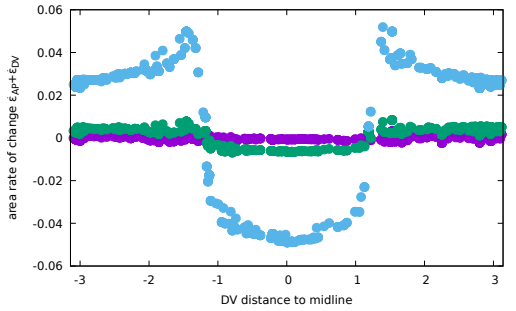

(*d*) Area rate of change

Figure 6: See caption on next page

Figure 6: Influence of the bulk viscosity on the convergence and extension of GB. (*a*) Flows calculated for (*top*) $\eta_b/\eta = 10^3$, (*center*) $\eta_b/\eta = 10^2$, (*bottom*) $\eta_b/\eta = 10$. While the posterior-wards flow at the GB posterior end is similar, the lateral flow is strongly affected with a much larger ventral-wards convergent flow along DV when the bulk viscosity is reduced to 10 (whereas no qualitative change is seen between 10^3 and 10^2). The position of the vortex center is also much modified for low bulk viscosity. (*b*) Rates of strain in the DV ($\updownarrow$ symbols) and AP ($\leftrightarrow$ symbols) directions for the three choices of η_b/η (*purple*, 10^3, *green*, 10^2, *cyan*, 10), as a function of AP coordinate x close to the midline ($y = 0.2R$). In the GB, DV rate is negative (convergence) and AP rate positive (extension). The DV rate of strain is increasingly negative for low bulk viscosity, indicating a stronger convergent flow, while the AP rate increases much less, indicating little change in the rate of GB extension. Posterior to the GB (AP coordinate $x \gtrsim 2$), the DV and AP strain rate values ramp and invert their sign, indicating that the direction of elongation swaps from AP to DV, which corresponds to the splayed velocity vectors seen at the limit of the GB in panel *a*. Anterior to the GB (AP coordinate $x \simeq -1$), the same effect is observed due to the obstacle of the cephalic furrow. (*c*) Rate of area change for the same choices of η_b/η, confirming that area decreases much more for lower bulk viscosity in the GB region. (*d*) Rate of area change for the same choices of η_b/η as a function of the DV distance to ventral midline, along a transverse cut midway along AP ($x = 0$). When η_b/η is sufficiently small to allow area variations, the GB region exhibits area reduction and dorsal region area increase.

---

to move relative to the cell apical membrane. At the tissue scale in GB extension, on the contrary, the cost of membrane deformations will be lumped in the viscosity of the apical continuum, but friction with perivitelline membrane may contribute.

The cephalic furrow acts as a guide for morphogenetic movements

In figure 3, it is seen that the flow follows the cephalic furrow in a parallel way. Thus we wondered whether the presence of the cephalic furrow could be of importance for the flow pattern observed. To test this, we performed the same simulation on two different meshes, one featuring the cephalic furrow and the other without it. It is seen in figure 8*e* that in the absence of a cephalic furrow, the flow at the anterior boundary of the GB does not deviated laterally but continues towards the anterior. The flow field is thus much more symmetrical than in the case with a cephalic furrow, figure 8*b*. From purely mechanical considerations, it is expected that if both the geometry of the embryo and the myosin expression are symmetrical, then the flow will be symmetrical too (see figure 8*d* for a verification of this). In real embryos, two sources of asymmetry arise: the invagination in the midgut, although blocking it does not completely suppress the posterior-wise extension of GB, and the offset of the planar-polarised myosin recruitment pattern towards the posterior. Our results suggest that another asymmetry could originate from the geometry of the embryo, with the cephalic furrow acting as a barrier resisting flow towards the anterior. Indeed, if one introduces this geometric asymmetry in the otherwise perfectly symmetrical embryo, the flow is strongly asymmetric towards the posterior end, figure 8*a*.

Discussion

A mechanical scenario for GB extension

Our simulation results confirm that either of the two mechanisms whose elimination was seen to correlate with a reduction of GB extension [9, 10, 11, 12, 13] can be the direct mechanical cause of a flow towards the posterior in the GB. The results in figure 5 indicate that although the GB extends whenever at least one of the effects is present, the precise flow patterns should differ in these different cases. An important and obvious next step is therefore to obtain experimentally the distribution and polarisation of myosin on the entire embryo surface, for example using SPIM, for different mutants, which should allow us to estimate the

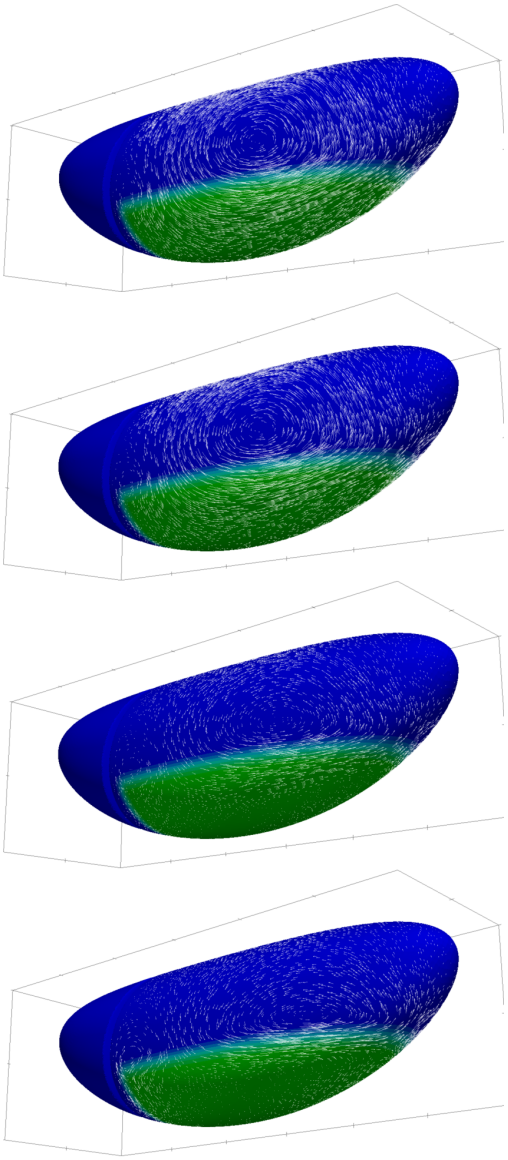

(a)

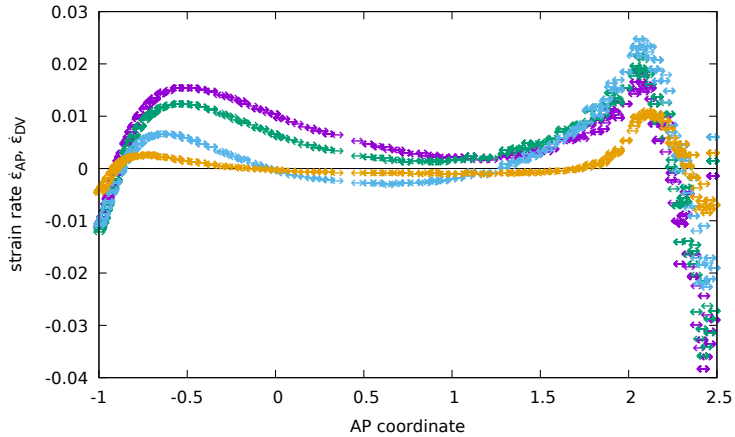

(b) AP strain rate

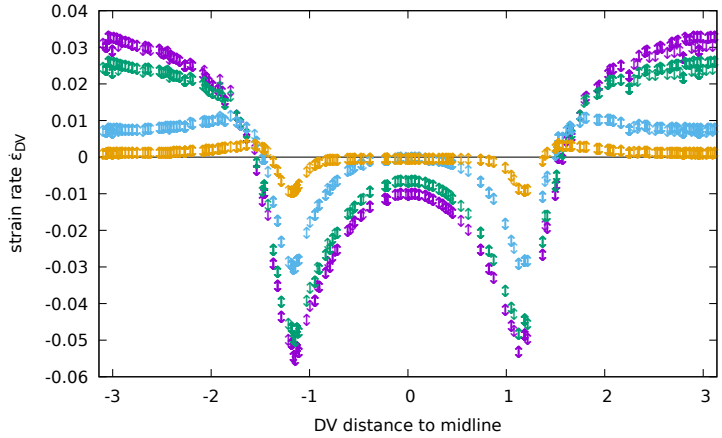

(c) DV strain rate

Figure 7: See caption on next page

Figure 7: Friction with vitelline membrane and/or cytosol and yolk modifies the flow pattern. (*a*) Global flow pattern. Parameters are the same as in figure 3, but the hydrodynamic length varies between $\Lambda = 10R$ (*top*), $\Lambda = R$ (reprinted from figure 3), $\Lambda = R/10$, and $\Lambda = R/100$ (*bottom*). In all cases the GB extends posteriorly. In the cases of small hydrodynamic length, convergence and extension flow occur mostly in regions where there is a gradient of contractility. Overall, friction renders the effect of actomyosin activity more local to regions where they exhibit a variation, hence vortex structures are more localised next to these regions with higher friction and have less influence in regions of uniform actomyosin activity (dorsally or close to ventral midline e.g.) (*b*) Rates of strain in the AP direction for the four choices of Λ/R (*purple*, $10R$, *green*, 1, *cyan*, 1/10 and *orange*, 1/100), as a function of AP coordinate x close to the midline ($y = 0.2R$). The overall magnitude of strain decreases with increased friction, as an increasing part of the energy provided by myosin activity needs to overcome friction in addition to deforming the cell apices. The rate of strain is uniformly positive (elongation) only when Λ is close to unity or smaller, else a region of shortening appears in the central part of GB. (Note that since area change is close to zero, the DV strain value is very close and opposite to the value of AP strain everywhere.) (*c*) Rate of strain in the DV direction for the four choices of Λ, as a function of AP coordinate x close to the midline ($y = 0.2R$). DV rate of strain always peaks close to the boundary of the GB area where myosin is active, in relative terms the peak is more pronounced for large frictions. Dorsally, there is always a positive DV rate of strain, indicating a DV elongation due to the pull of the neighbouring converging GB. This is matched with an AP shortening of a similar magnitude. Ventrally, the negative rate of strain (indicating convergence) is observed to decay when the hydrodynamic length becomes small, in that case the DV narrowing is limited to a narrow band at the DV edge of the GB. This localisation effect of small hydrodynamic length is also seen for the dorsal DV elongation, but to lesser extent.

---

parameters and test the predictive power of the model. However, our theoretical work already sheds light on the fundamental mechanisms at play and how they integrate in the complex 3D geometry of the embryo to yield the morphogenetic events that are observed.

Based on our simulations and the timings reported in the literature, we can indeed articulate a mechanical scenario for GB extension. The endoderm contraction that leads to PMG invagination, the first event correlated with GB extension [13, Fig. 4B], starts 1 to 4 minutes before the onset of GB extension can be detected. The corresponding simulation is shown in figure 5*e*, PMG contraction generates a flow towards the posterior that does extend the posterior half of the germband but decays rapidly in space. This is consistent with what is observed e.g. in *Kruppel* mutants [13]. The presence of the cephalic furrow for this extension does not have a strong influence there, see figure 8*f*. Thereafter, from shortly before the onset and in the course of GB extension, myosin becomes increasingly planar-polarised [25]. The direct consequence of this is a lateral flow from dorsal to ventral, causing *convergence*, that is, a negative rate of strain of GB along the DV direction. Due to a rather large value of η_{b}, which corresponds to the in-plane compressibility viscosity of actomyosin, this causes GB extension, see figure 6. Experimental evidence of such an in-plane low compressibility exists [11, 12], although it is not clear whether this is a passive mechanical property of the actomyosin cortex or an active one [26, 12]. In the absence of the cephalic furrow, figure 8*e*, this extension occurs evenly in the anterior and posterior directions, in presence of the cephalic furrow, the viscous cost of flowing around the posterior end is much less than the cost of flowing into the furrow, and planar polarisation driven GB extension is biased towards posterior, even if the contribution of PMG invagination is not accounted for, figure 3.

Cellularisation of GB may not be necessary for convergence and extension of planar-polarised tissue

The two prominent features in which cellularisation is involved in GB extension in WT *Drosophila* are the planar-polarised recruitment of myosin, which preferentially enriches DV-oriented junctions, and the medio-

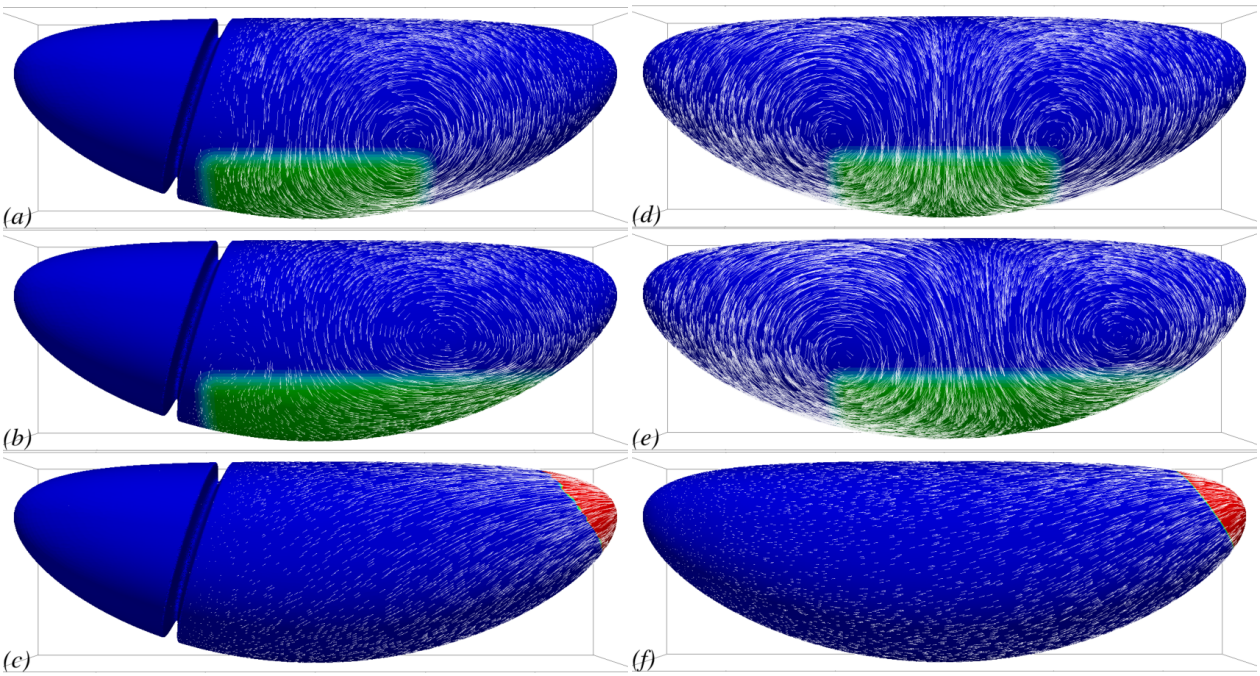

Figure 8: Cephalic furrow (CF) can guide GB extension to be mostly posterior-wards. Lateral view of flow fields generated by myosin contractility in the presence (*a*–*c*) or absence (*d*–*f*) of a cephalic furrow. (*a*,*d*) With a hypothetical symmetric planar-polarised myosin activity, the presence of CF orients the flow towards posterior whereas it is perfectly symmetric in its absence. (*b*,*e*) With a realistic asymmetric planar-polarised myosin activity, the presence of CF still has a major role in orienting the flow towards posterior. Although the asymmetric myosin patterning induces a asymmetric flow in the absence of the CF, the flow is not biased towards posterior. (*c*,*f*) The flow created by PMG invagination is much less sensitive to the presence of CF.

lateral cell intercalations [31, 9, 10]. Because the DV-oriented junctions present both the characteristics of being enriched in myosin and of undergoing shrinkage to lead to intercalation, these two effects have so far been studied in association. However, some mutants such as *eve* that lack planar polarisation of myosin can still exhibit some cell intercalation, although to a much lesser proportion than cell shape changes [11]. Here using our modelling approach we can envision the reverse case of studying convergence-extension due to planar-polarised myosin activity but without explicit cell intercalation. We show that the anisotropy of planar-polarised myosin activity is sufficient to explain convergence-extension, without the need for an intercalation mechanism.

Indeed, from the above, we conclude that a mechanical model that does not involve individual cells but only a continuum standing for the apical acto-myosin connected from cell to cell by apical junctions can produce a flow with similarities to GB extension. Cellularisation is of course important for the planar polarisation of myosin in the GB, and it is observed that acellular embryos do not exhibit myosin polarisation [13]. Here, planar polarisation is introduced in the mechanical model by means of an anisotropic contractility action of myosin $\boldsymbol{\sigma}_{\mathbf{a}}$. The fact that no further account of the cellularisation of the embryo is necessary in the model suggests that at the tissue scale, one can address morphogenetic questions by considering ensemble displacements. In this approach, the effect of cell intercalation, which is governed by planar-polarised junctional myosin, is thus not directly taken into account, but rather encapsulated in a global tissue strain rate and its associate viscosities η and η_{b}, which also include the cell deformation [15].

This tissue strain rate $\dot{\boldsymbol{\varepsilon}}$ and the corresponding tissue-scale tension $\boldsymbol{\sigma}$ are related by the constitutive relation, 2, which includes the contractility term $\boldsymbol{\sigma}_{\mathbf{a}}$ resulting from planar-polarised myosin activity, and is thus the only term bearing a trace of the embryo's cellularised organisation. The respective values taken by $\dot{\boldsymbol{\varepsilon}}$ and $\boldsymbol{\sigma}$ locally depend on the mechanical balance, i.e. both the local myosin activity and the tension transmitted by neighbouring tissue, see figure 2*d*. In the context of convergence-extension caused partly by invagination of the PMG, [13], it has been proposed that cell intercalation could relax the stress by allowing cell shape changes in a GB extended by an extrinsic force. Here we propose that the intrinsic planar-polarised contraction might still extend the GB in the absence of intercalation, and that intercalation could in that case too have for primary role the relaxation of the stress generated by the convergence and extension process.

Geometry-governed mechanical balance as a messenger in early morphogenesis

Planar-polarised myosin in the GB is known to generate a global flow at the surface of the embryo. Our simulations show that the global flow which is generated by such mechanical activity is dependent on the pre-existing geometry of the embryo, such as the presence or absence of the cephalic furrow. Thus, a prior morphogenetic movement such as cephalic furrow formation can affect further movements via mechanical interactions only, see figure 1*f*.

This "messaging" proceeds via the establishment of a different mechanical balance depending on the geometry of the embryo, rather than the diffusion of a morphogen, e.g. [32]. In the early embryo, the distance over which these forces are transmitted is likely to be much larger than in later organisms, as there is no extra-cellular matrix structure that will relieve actomyosin from part of the stress. Indeed, we find that the hydrodynamic length is likely to be at least the width of the GB, consistent with laser ablation results [30], which implies direct mechanical interaction at this scale.

This mechanical messaging behaves differently from biochemical messaging. Its speed of propagation is the speed of sound in the force-bearing structure, here, the actomyosin. It does not propagate in an isotropic way but in a more complex directional one, and contains directional information. Regions of interest within the embryo should thus not be treated as isolated systems, since a distant geometric property of the embryo can have a direct impact on the mechanical stress felt locally when intrinsic forces are being generated.

This prompts further development of computational tools such as the one we present. Tangential flows on curved surfaces are also observed in other epithelia (such as follicular epithelium of *Drosophila* ovaries), but is also relevant to cortical flows in single cells, prior to mitotic cleavage for example. Mechanical approaches of flat epithelia have shed light on many aspects of tissue growth and dynamics [33, 34, 35, 25], in particular at the scale of a few cells, which is the relevant one for cell rearrangements. At the other end of the spectrum

of tissue dynamics, 3D phenomenological models of shape changes during ventral furrow formation have been proposed [16]. Here we propose a first step in bridging the gap between these approaches, with the objective to be able to address complex morphogenetic events in their actual geometry, and thus to fully account for the influence of current morphology on the mechanical balance that leads to further morphogenetic movements.

Methods

Lagrange multiplier approach for tangential flows

Equation equation 3 must be resolved for velocities $\boldsymbol{v}$ tangential to the surface Γ, which corresponds to the continuum formed by the apical actomyosin cortices of cells and adherens junctions. This constraint can be written as $\boldsymbol{v} \in \boldsymbol{V}_t = \left\{ \boldsymbol{w} \in \left(H^1(\Gamma)\right)^3 \mid \boldsymbol{w} \cdot \boldsymbol{n} = 0 \right\}$, where $\left(H^1(\Gamma)\right)^3$ is the set of vector-valued functions defined on Γ whose differential is square-integrable, and $\boldsymbol{n}$ is the outer normal to Γ. Using an energetic formulation, it can then be shown that equation 3 is equivalent to the constrained minimisation:

$$\boldsymbol{v} = \arg \inf_{\boldsymbol{w} \in \boldsymbol{V}_t} E(\boldsymbol{w}) \tag{4}$$

where E is the rate of energy dissipation in the tissue, namely:

$$E(\boldsymbol{w}) = \int_\Gamma \frac{c_\mathrm{f}}{2} |\boldsymbol{w}|^2 \,\mathrm{ds} + \int_\Gamma \eta \left|\dot{\boldsymbol{\varepsilon}}(\boldsymbol{w})\right|^2 \mathrm{ds} + \int_\Gamma \frac{\lambda}{2} \left|\nabla_\Gamma \cdot \boldsymbol{w}\right|^2 \mathrm{ds} - \int_\Gamma \boldsymbol{f} \cdot \boldsymbol{w} \,\mathrm{ds}$$

and $\boldsymbol{f} = \boldsymbol{\nabla}_\Gamma \cdot \boldsymbol{\sigma}_\mathbf{a}$. Our approach is to introduce a vector field $\boldsymbol{\theta}$ that will act as a Lagrange multiplier to constrain the velocities $\boldsymbol{v}$ to be tangential. This field $\boldsymbol{\theta}$ can be interpreted as the force needed to prevent normal deformations. In order to do this, we first define $\boldsymbol{\theta}$ by $\boldsymbol{\theta} = \gamma \boldsymbol{L}(\boldsymbol{v})$ where $\boldsymbol{L}(\boldsymbol{v}) = (\boldsymbol{v} \cdot \boldsymbol{n})\, \boldsymbol{y} - \nabla_\Gamma \boldsymbol{v} \cdot \boldsymbol{n}$, $\boldsymbol{y}$ is the curvature vector, and γ is a strictly positive parameter. Then we note that $\boldsymbol{V}_t = \ker \boldsymbol{L}$. The problem can now be rewritten as an unconstrained saddle-point problem :

$$(\boldsymbol{v}, \boldsymbol{\theta}) = \arg \inf_{\boldsymbol{w} \in \boldsymbol{V}} \sup_{\boldsymbol{\xi} \in \boldsymbol{\Xi}} E(\boldsymbol{w}) + \int_\Gamma \left(\boldsymbol{L}(\boldsymbol{w}) - \frac{1}{\gamma} \boldsymbol{\xi} \right) \cdot \boldsymbol{\xi} \,\mathrm{ds}$$

where $\boldsymbol{V} = \left(H^1(\Gamma)\right)^3$ and $\boldsymbol{\Xi} = \left(L^2(\Gamma)\right)^3$, the set of square-integrable vector fields. We further introduce the surface pressure p which enforces the finite compressibility of the actomyosin in the tangential plane, $p = -\lambda \nabla_\Gamma \cdot \boldsymbol{v}$. We can then write the problem as :

$$(\boldsymbol{v}, p, \boldsymbol{\theta}) = \arg \inf_{\boldsymbol{w} \in \boldsymbol{V}} \sup_{\substack{q \in Q \\ \boldsymbol{\xi} \in \boldsymbol{\Xi}}} \mathcal{L}(\boldsymbol{w}, q, \boldsymbol{\xi})$$

where $Q = L^2(\Gamma)$,

$$\mathcal{L}(\boldsymbol{w}, q, \boldsymbol{\xi}) = \frac{1}{2} a(\boldsymbol{w}, \boldsymbol{w}) + b_1(\boldsymbol{w}, q) - \frac{1}{2} c_1(q, q) + b_2(\boldsymbol{w}, \boldsymbol{\xi}) - \frac{1}{2} c_2(\boldsymbol{\xi}, \boldsymbol{\xi}) - \ell(\boldsymbol{w})$$

and a, b_1, b_2, c_1 and c_2 are the bilinear forms defined by :

$$\begin{aligned}
a(\boldsymbol{w}, \boldsymbol{w}) &= \int_\Gamma c_\mathrm{f} \boldsymbol{w} \cdot \boldsymbol{w} \,\mathrm{ds} + \int_\Gamma 2\eta \dot{\boldsymbol{\varepsilon}}(\boldsymbol{w}) : \dot{\boldsymbol{\varepsilon}}(\boldsymbol{w}) \,\mathrm{ds}, \\
b_1(\boldsymbol{w}, q) &= \int_\Gamma -q \nabla_\Gamma \cdot \boldsymbol{w} \,\mathrm{ds}, \quad c_1(p, q) = \int_\Gamma \frac{1}{\lambda} pq \,\mathrm{ds}, \\
b_2(\boldsymbol{w}, \boldsymbol{\xi}) &= \int_\Gamma \boldsymbol{L}(\boldsymbol{w}) \cdot \boldsymbol{\xi} \,\mathrm{ds}, \quad c_2(\boldsymbol{\theta}, \boldsymbol{\xi}) = \int_\Gamma \frac{1}{\gamma} \boldsymbol{\theta} \cdot \boldsymbol{\xi} \,\mathrm{ds}
\end{aligned}$$

and ℓ is the linear form define by : $\ell(\boldsymbol{w}) = \int_\Gamma \boldsymbol{f} \cdot \boldsymbol{w} \, \mathrm{ds}$. The saddle point can then be characterized as the solution of the linear problem :

$$\begin{array}{ccccccccc} a(\boldsymbol{v},\boldsymbol{w}) & + & b_1(\boldsymbol{w},p) & + & b_2(\boldsymbol{w},\boldsymbol{\theta}) & = & \ell(\boldsymbol{w}) & & \forall\, \boldsymbol{w} \in \left(H^1(\Gamma)\right)^3 \\ b_1(\boldsymbol{v},q) & - & c_1(p,q) & & & = & 0 & & \forall\, q \in Q \\ b_2(\boldsymbol{v},\boldsymbol{\xi}) & & & - & c_2(\boldsymbol{\theta},\boldsymbol{\xi}) & = & 0 & & \forall\, \boldsymbol{\xi} \in \Xi. \end{array}$$

Mixed finite element approach

We solve the saddle point problem using the finite element method. This requires us to introduce a mesh Γ_h approximating Γ. We use a triangular tessellation of second order, i.e. elements are curved triangles described by a quadratic transformation and whose largest dimension is smaller than the mesh size h. This ensures that the distance between any point of Γ_h and Γ is at most Ch^3, where C is a constant independent of h. Using this mesh, we define discrete functional spaces $\boldsymbol{V}_h$, $\boldsymbol{\Xi}_h$ for vector fields $\boldsymbol{v}_h$, $\boldsymbol{\theta}_h$ and Q_h of scalar field p_h. We approach the saddle point problem using the following formulation :

$$\begin{array}{ccccccccc} a_h(\boldsymbol{v}_h,\boldsymbol{w}_h) & + & b_{1,h}(\boldsymbol{w}_h,p_h) & + & b_{2,h}(\boldsymbol{w}_h,\boldsymbol{\theta}_h) & = & \ell_h(\boldsymbol{w}_h) & & \forall\, \boldsymbol{w}_h \in \boldsymbol{V}_h \\ b_{1,h}(\boldsymbol{v}_h,q_h) & - & c_{1,h}(p_h,q_h) & & & = & 0 & & \forall\, q_h \in Q_h \\ b_{2,h}(\boldsymbol{v}_h,\boldsymbol{\xi}_h) & & & - & c_{2,h}(\boldsymbol{\theta}_h,\boldsymbol{\xi}_h) & = & 0 & & \forall\, \boldsymbol{\xi}_h \in \boldsymbol{\Xi}_h \end{array}$$

where $a_h, b_{1,h}, b_{2,h}, c_{1,h}$ and $c_{2,h}$ are bilinear forms approximating the original forms, defined by :

$$\begin{aligned} a_h(\boldsymbol{v}_h,\boldsymbol{w}_h) &= \int_{\Gamma_h} c_\mathrm{f} \boldsymbol{v}_h \cdot \boldsymbol{w}_h \, \mathrm{ds}_h + \int_{\Gamma_h} 2\eta \dot{\boldsymbol{\varepsilon}}_h(\boldsymbol{v}_h) : \dot{\boldsymbol{\varepsilon}}_h(\boldsymbol{w}_h) \, \mathrm{ds}_h, \\ b_{1,h}(\boldsymbol{w}_h,q_h) &= \int_{\Gamma_h} -q_h \nabla_{\Gamma_h} \cdot \boldsymbol{w}_h \, \mathrm{ds}_h, \quad c_{1,h}(p_h,q_h) = \int_{\Gamma_h} \frac{1}{\lambda} p_h q_h \, \mathrm{ds}_h, \\ b_{2,h}(\boldsymbol{w}_h,\boldsymbol{\xi}_h) &= \int_{\Gamma_h} \boldsymbol{L}_h(\boldsymbol{w}_h) \cdot \boldsymbol{\xi}_h \, \mathrm{ds}_h, \quad c_{2,h}(\boldsymbol{\theta}_h,\boldsymbol{\xi}_h) = \int_{\Gamma_h} \frac{1}{\gamma} \boldsymbol{\theta}_h \cdot \boldsymbol{\xi}_h \, \mathrm{ds}_h \end{aligned}$$

and ℓ_h is the linear form defined by $\ell_h(\boldsymbol{v}_h) = \int_{\Gamma_h} \boldsymbol{f}_h \cdot \boldsymbol{v}_h \, \mathrm{ds}_h$. The choice of the finite element spaces cannot be made arbitrarily because it is a mixed problem. It requires a suitable choice in order for the discrete problem converges towards the saddle point problem. Indeed, the discrete problem must verify two conditions called *inf–sup* or *Brezzi–Babuska* conditions (see [36]) : first between the spaces $\boldsymbol{V}_h$ and Q_h through the bilinear form $b_{1,h}$, then between the spaces $\boldsymbol{V}_h$ and $\boldsymbol{\Xi}_h$ through the bilinear form $b_{2,h}$. In the absence of theoretical results on spaces that may verify these conditions, the idea is to produce compatible mixed finite element combinations in order to obtain the convergence. For this, we guided our choice by similarity with choices for which *inf–sup* conditions are verified in the case of classical problems (such as the three-dimensional Stokes problem).

Numerical validation

Next, finite element spaces $\boldsymbol{V}_h$, Q_h and $\boldsymbol{\Xi}_h$ must be specified. We base them on a triangular tesselation of the surface Γ (see next section) and choose Lagrange finite elemnts of degree 3 for $\boldsymbol{V}_h$, 2 for Q_h and $\boldsymbol{\Xi}_h$. We then check that this choice leads to a convergent approximation of the solution of equation 3. In order to do so, we make an arbitrary choice of a velocity field on an arbitrary surface (a sphere), and calculate analytically the prestress that would be needed to achieve such a velocity field. We then run simulations on a series of meshes of decreasing triangle size h and monitor the evolution of the error $\boldsymbol{v} - \boldsymbol{v}_h$. We show [19] that this decreases quadratically when h decreases, leading to pointwise errors (i.e., in L^∞ norm) smaller than 10^{-3} for all meshes of more than 10000 elements ($h = 0.05$). For these numerical tests, we chose : $c_\mathrm{f} = 10^{-5}$, $\eta = 1$, $\lambda = 10^3$ and $\gamma = 10^7$.

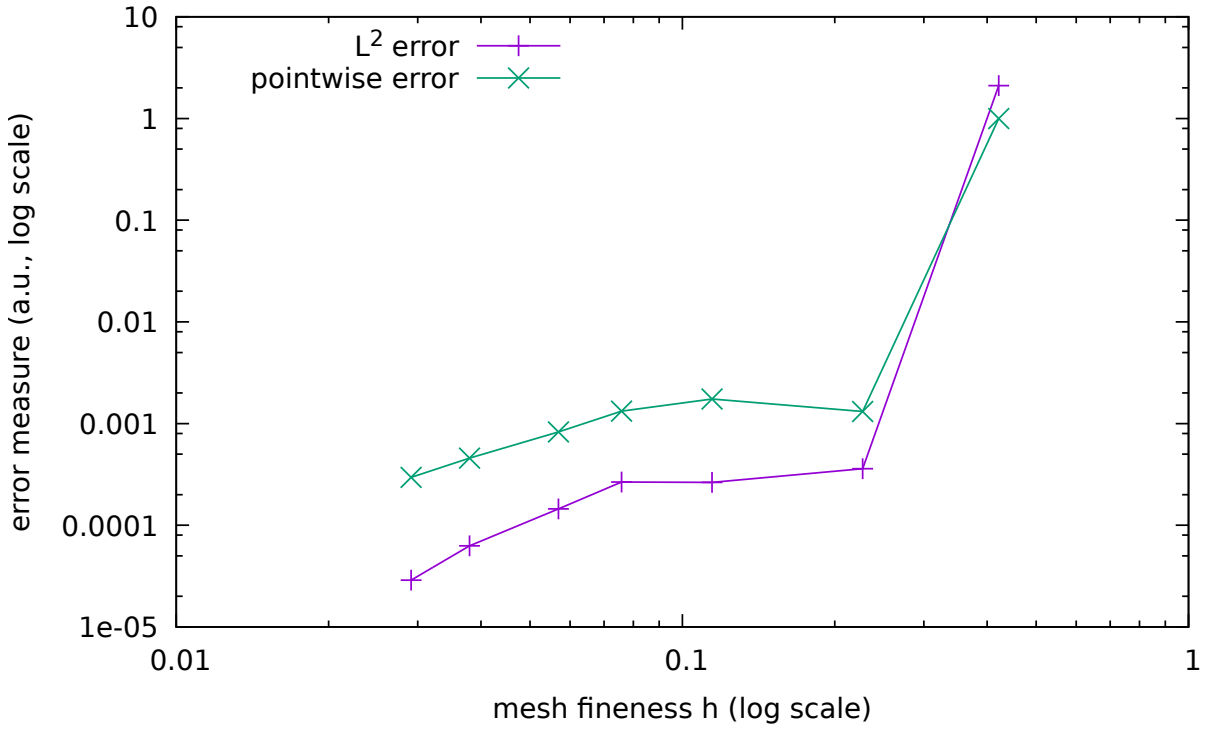

Figure 9: Convergence test. The mesh is refined (from right to left) and the error on an arbitrary flow field is seen to decrease. L^2 error is the overall squared difference of calculated minus original velocity vectors, pointwise (L^∞) error is the length of the largest difference between calculated and original velocity vectors over the whole mesh.

Finite element mesh of the *Drosophila* embryo and resolution

We first describe the embryo shape with an analytical function, and then introduce a procedure to create a finite element mesh which will be fine enough to capture geometric details such as the cephalic furrow, while remaining of reasonable size in terms of the number of triangles (since the computational cost of our algorithms increases like $N\log(N)$ with number of triangles N).

The analytical function describing the embryo shape $\Gamma = \{\phi(x,y,z) = 0\}$ is chosen as:

$$\phi(x,y,z) = 1 - \sqrt{\left(\frac{x}{R_{AP}}\right)^2 + \left(\frac{y}{R_{DV}}\right)^2 + \left(\frac{z - \frac{1}{2}c_{AP}x^2}{R_{DV}}\right)^2} + D_{CF}\psi_{CF}\left(\frac{x - S_{CF}z - x_{CF}}{W_{CF}}\right)$$

where R_{AP} is the half-length of the embryo in AP, R_{DV} its maximum radius in a transverse cut, c_{AP} a curvature parameter corresponding to the curvature of the main axis of the embryo (defined as the locus of the center of all transverse cuts), and parameters indexed with CF correspond to the cephalic furrow. When $D_{CF} = 0$, the cephalic furrow is absent, and the geometry corresponds to an ellipsoid of major axis along x, with radius R_{AP}, and minor axes along y and z of equal radii R_{DV}. The curvature parameter flattens the dorsal side ($z > 0$). We take $R_{DV} = 1$ as the reference adimensional length, $R_{AP} = 3R_{DV}$ and $c_{AP} = 0.1/R_{DV}$, which leads to a shape close to the one of actual embryos.

The cephalic furrow depth is described by $D_{CF} = 0.1R_{DV}$, its position along the x axis in the mid-coronal plane $z = 0$ is given by $x_{CF} = -1.2R_{DV}$, and its inclination with respect to the (y,z) transverse planes is set by $S_{CF} = 0.3$. The cephalic furrow has a total width $W_{CF} = 0.1R_{DV}$ (exaggerated compared to real embryos, since a very thin and sharp feature would increase tremendously the computational cost), its shape is described by the function

$$\psi_{CF}(s) = \begin{cases} \exp\left(-\frac{2}{1-s^2} + 2\right) & \text{if } |s| < 1 \\ 0 & \text{else} \end{cases}$$

which is infinitely derivable, leading to a very smooth profile.

The mesh generation is delegated to `gmsh` software, and the meshes used have around 46000 elements. The numerical resolution of the problem on this mesh is implemented in the open-source free software environment `rheolef` [37].

Acknowledgements

Authors thank Bénédicte Sanson, Claire Lye and Guy Blanchard for many fruit fly discussions. JE also thanks Alexandre Kabla, Alexander Fletcher and Jonathan Fouchard. All the computations presented in this paper were performed using the Cactus platform of the CIMENT infrastructure (https://ciment.ujf-grenoble.fr), which is supported by Région Rhône-Alpes (GRANT CPER07-13 CIRA: http://www.ci-ra.org). Authors would like to thank Philippe Beys who manages the platform. Authors thank Région Rhône-Alpes (CIBLE and IXXI, all authors; CMIRA, JE), MD thanks Malian government and French embassy in Bamako "Bourse d'Excellences" programme, LIPHY and LJK (CNRS and Univ. Grenoble Alpes) for financial support. MD and JE thank ANR-12-BS09-0020-01 "Transmig" and ANR-11-LABX-0030 "Tec21", and are members of GDR 3570 *MécaBio* and GDR 3070 *CellTiss* of CNRS. JE thanks the Isaac Newton Institute for Mathematical Sciences for its hospitality during the programme *Coupling Geometric PDEs with Physics for Cell Morphology, Motility and Pattern Formation* supported by EPSRC Grant Number EP/K032208/1.

References

[1] P. E. Young, A. M. Richman, A. S. Ketchum, and D. P. Kiehart. Morphogenesis in Drosophila requires nonmuscle myosin heavy chain function. *Genes Dev.*, 7:29–41, 1993.

[2] T. Yeung, P. C. Georges, L. A. Flanagan, B. Marg, M. Ortiz, M. Funaki, N. Zahir, W. Ming, V. Weaver, and P. A. Janmey. Effects of substrate stiffness on cell morphology, cytoskeletal structure, and adhesion. *Cell Motil. Cytoskeleton*, 60:24–34, 2005.

[3] N. Desprat, W. Supatto, P.-A. Pouille, E. Beaurepaire, and E. Farge. Tissue deformation modulates twist expression to determine anterior midgut differentiation in drosophila embryos. *Developmental Cell*, 15:470–477, 2008.

[4] A. Zemel, F. Rehfeldt, A. E. X. Brown, D. E. Discher, and S. A. Safran. Optimal matrix rigidity for stress-fibre polarization in stem cells. *Nature Phys.*, 6:468–473, 2010.

[5] J. Étienne, J. Fouchard, D. Mitrossilis, N. Bufi, P. Durand-Smet, and A. Asnacios. Cells as liquid motors: Mechanosensitivity emerges from collective dynamics of actomyosin cortex. *Proc. Natl. Acad. Sci. USA*, 112:2740–2745, 2015.

[6] C. M. Lye and B. Sanson. Tension and epithelial morphogenesis in *drosophila* embryos. In Michel Labouesse, editor, *Forces and Tension in Development*, volume 95 of *Curr. Topics Dev. Biol.*, pages 145–187. Elsevier, 2011.

[7] N. D. Czerniak, K. Dierkes, A. D'Angelo, J. Colombelli, and J. Solon. Patterned contractile forces promote epidermal spreading and regulate segment positioning during Drosophila head involution. *Curr. Biol.*, 26:1895–1901, 2016.

[8] M. Costa, D. Sweeton, and E. Wieschaus. *Gastrulation in Drosophila: Cellular mechanims of morphogenetic movements*, pages 425–465. 1993.

[9] C. Bertet, L. Sulak, and T. Lecuit. Myosin-dependent junction remodelling controls planar cell intercalation and axis elongation. *Nature*, 429:667, 2004.

[10] J. T. Blankenship, S. T. Backovic, J. S. Sanny, O. Weitz, and J. A. Zallen. Multicellular rosette formation links planar cell polarity to tissue morphogenesis. *Dev. Cell*, 11:459–470, 2006.

[11] L. C. Butler, G. B. Blanchard, A. J. Kabla, N. J. Lawrence, D. P. Welchman, L. Mahadevan, R. J. Adams, and B. Sanson. Cell shape changes indicate a role for extrinsic tensile forces in drosophila germ-band extension. *Nature Cell Biol.*, 2009.

[12] C. Collinet, M. Rauzi, P.-F. Lenne, and T. Lecuit. Local and tissue-scale forces drive oriented junction growth during tissue extension. *Nature Cell Biol.*, 17:1247–1258, 2015.

[13] C. Lye, G. Blanchard, H. Naylor, L. Muresan, J. Huisken, R. Adams, and B. Sanson. Mechanical coupling between endoderm invagination and axis extension in drosophila. *PLoS Biol.*, in press, 2015.

[14] A. G. Fletcher, M. Osterfield, R. E. Baker, and Stanislav Y. Shvartsman. Vertex models of epithelial morphogenesis. *Biophys. J.*, 106:2291–2304, 2014.

[15] G. B. Blanchard, A.J. Kabla, N.L. Schultz, L.C. Butler, B. Sanson, N. Gorfinkiel, L. Mahadevan, and R.J. Adams. Tissue tectonics: morphogenetic strain rates, cell shape change and intercalation. *Nature Methods*, 6:458–464, 2009.

[16] M. Rauzi, A. H. Brezavscek, P. Ziherl, and M. Leptin. Physical models of mesoderm invagination in drosophila embryo. *Biophys. J.*, 105:3–10, 2013.

[17] R. Allena, A.-S. Mouronval, and D. Aubry. Simulation of multiple morphogenetic movements in the Drosophila embryo by a single 3D finite element model. *J. Mech. Behavior Biomech. Mat.*, 3:313–323, 2010.

[18] I. Nitschke, A. Voigt, and J. Wensch. A finite element approach to incompressible two phase flow on manifolds. *J. Fluid Mech.*, 2012.

[19] M. Dicko. *Méthodes numériques pour la résolution d'EDP sur des surfaces. Application dans l'embryogenèse*. PhD thesis, Univ. Grenoble, 2016.

[20] B. He, K. Doubrovinski, O. Polyakov, and E. Wieschaus. Apical constriction drives tissue-scale hydrodynamic flow to mediate cell elongation. *Nature*, 2014.

[21] J. T. Blankenship and E. Wieschaus. Two new roles for the drosophila ap patterning system in early morphogenesis. *Dev.*, 128:5129, 2001.

[22] M.E. Gurtin, J. Weissmuller, and F. Larche. The general theory of curved deformable interfaces in solids at equilibrium. *Philos. Mag. A*, 78:1093–1109, 1998.

[23] P. F. Machado, J. Duque, J. Étienne, A. Martinez-Arias, G. B. Blanchard, and N. Gorfinkiel. Emergent material properties of developing epithelial tissues. *BMC Biol.*, 13:98, 2015.

[24] C. Roux, A. Duperray, V. M. Laurent, R. Michel, V. Peschetola, C. Verdier, and J. Étienne. Prediction of traction forces of motile cells. *J. R. Soc. Interface Focus*, 6:20160042, 2016.

[25] R. J. Tetley, G. B. Blanchard, A. G. Fletcher, R. J. Adams, and B. Sanson. Unipolar distributions of junctional myosin ii identify cell stripe boundaries that drive cell intercalation throughout drosophila axis extension. *eLife*, 5:e12094, 2016.

[26] J. K. Sawyer, W. Choia, K.-C. Junga, L. Heb, N. J. Harris, W. Choia, K.-C. Junga, L. Heb, and N. J. Harris Peifer. A contractile actomyosin network linked to adherens junctions by canoe/afadin helps drive convergent extension. *Mol. Biol. Cell*, 22:2491, 2011.

[27] J. Huisken and D. Y. Stainier. Selective plane illumination microscopy techniques in developmental biology. *Devel.*, 136:1963–1975, 2009.

[28] M. Rauzi, U. Krzic, T. E. Saunders, M. Krajnc, P. Ziherl, L. Hufnagel, and M. Leptin. Embryo-scale tissue mechanics during drosophila gastrulation movements. *Nature Comm.*, 6:8677, 2015.

[29] X. Ma, H. E. Lynch, P. C. Scully, and M. S. Hutson MS. Probing embryonic tissue mechanics with laser hole drilling. *Phys Biol.*, 6:036004, 2009.

[30] A. Saha, M. Nishikawa, M. Behrndt, C.-P. Heisenberg, F. Juelicher, and S. W. Grill. Determining physical properties of the cell cortex. *Biophys. J.*, 110:1421–1429, 2016.

[31] K. D. Irvine and E. Wieschaus. Cell intercalation during drosophila germband extension and its regulation by pair-rule segmentation genes. *Development*, 120:827–841, 1994.

[32] A. D. Lander. Morpheus unbound: Reimagining the morphogen gradient. *Cell*, 128:245–256, 2007.

[33] J. A. Glazier and F. Graner. Simulation of the differential adhesion driven rearrangement of biological cells. *Phys. Rev. E*, 47:2128–2154, 1993.

[34] M. Rauzi, P. Verant, T. Lecuit, and P.-F. Lecuit. Nature and anisotropy of cortical forces orienting drosophila tissue morphogenesis. *Nat. Cell. Biol.*, 10:1401–1410, 2008.

[35] S. Titli, C. Gay, F. Graner, P. Marcq, F. Molino, and P. Saramito. Colloquium: Mechanical formalisms for tissue dynamics. *Eur. Phys. J. E*, 38:33, 2015.

[36] Franco Brezzi and Michel Fortin. *Mixed and hybrid finite element methods*. Springer-Verlag New York, Inc., New York, NY, USA, 1991.

[37] P. Saramito, N. Roquet, and J. Étienne. `rheolef`, a C++ finite element environment. Technical report, CNRS, 2003–2014. http://www-lmc.imag.fr/lmc-edp/Pierre.Saramito/rheolef.